Suppressing Formation of Zn—Mn—O Phases by In Situ Ti Decoration of MnO_2 for Long Lifespan MnO_2-Zn Battery

*Qiaohui Duan, Yiyi Zheng, Yu Zhou, Shuyu Dong, Calvin Ku, Patrick H.-L. Sit, and Denis Y. W. Yu**

Mildly-acidic MnO_2-Zn batteries are considered as a promising alternative for large-scale energy storage systems for their low toxicity, high safety, and low cost. Though, the degradation of MnO_2 with cycling still hinders the further development of the batteries. In this study, it is observed that the decrease in available capacity of MnO_2 with charge and discharge is accompanied by a structural transformation with the emergence of Zn—Mn—O phases. An electrodeposition test indicates that the Zn—Mn—O phase is formed from a co-precipitation of Zn and Mn during the charge process. Further, the structural change of MnO_2 is suppressed and its cycle stability is improved with the addition of $TiOSO_4$ as a facile electrolyte additive. As a result, under a current of 1200 mA g^{-1}, the MnO_2 electrode still gives a capacity of 230 mAh g^{-1} for over 1500 cycles. Capacity retention is 75% after 10 000 cycles under a current rate of 4800 mA g^{-1}. These findings provide fundamental insights on the degradation mechanism of MnO_2 and a new strategy to improve the electrochemical performance of aqueous MnO_2-Zn batteries.

1. Introduction

Aqueous rechargeable Zn-ion batteries (ARZIBs) are promising for grid-scale energy storage applications owing to the merits in abundant Zn source, intrinsic safety, and low cost.[1–3] Among the different cathode materials, MnO_2 is attractive because it is environmental friendly, available in large quantity, and also has high capacity.[4,5]

MnO_2, however, undergoes fast capacity fading with cycling.[6] The reversibility of the MnO_2-Zn system is greatly enhanced with the introduction of a Mn^{2+} additive into the mild acidic electrolyte, as it is claimed that the additive can suppress the dissolution of Mn^{2+} from the MnO_2 active material.[7] Though, capacity fading is still observed with Mn^{2+} additive into the electrolyte.[8–10] Thus, there is another mode of degradation that governs the long-term stability of MnO_2.

Formation of new phases upon cycling was reported as one of the causes of the poor electrochemical reversibility for different MnO_2-based polymorphs.[11–13] So far, many strategies such as surface coatings,[14–16] designing different MnO_2 morphologies and crystal structures,[17,18] introducing vacancies and dopants,[19–21] and electrode additive [22] etc. were proposed to overcome the issue. However, most of the reported works were only able to demonstrate stable cycling performances under high current rate with low capacity utilization (e.g., <150 mAh g^{-1} over 1000 cycles), as the MnO_2-Mn^{2+} dissolution-deposition reaction during each cycle would form new MnO_2 that is different from the originally designed MnO_2 structure.[23] For practical applications, it is desirable to find an alternative method to suppress the formation of new phases to maintain a high capacity utilization of over 200 mAh g^{-1} for extended number of cycles.

In general, it is recognized that MnO_2 undergoes two different reactions during charge and discharge: 1) H^+ (de)insertion reaction[8,24] with $MnO_2 + H^+ + e^- \rightleftharpoons HMnO_2$ *or* $MnOOH$ and 2) MnO_2-Mn^{2+} electro-dissolution/deposition reaction [25,26] with $MnO_2 + 4H^+ + 2e^- \rightleftharpoons Mn^{2+} + 2H_2O$. In this work, we first quantify the contribution of the two reactions to the observed capacity of electrolytic manganese dioxide (EMD), showing that both reactions occur simultaneously. Upon cycling, though, X-ray diffraction (XRD) analyses show that the original EMD phase disappears with the gradual emergence of $ZnMn_2O_4$ and $ZnMn_3O_7$ phases in the electrode, leading to capacity loss. These new Zn-containing phases are formed during a co-deposition of Mn^{2+} and Zn^{2+} during charging, as verified by an electrodeposition test of EMD onto a cathode-free carbon nanotube (CNT) electrode. We further demonstrate that the addition of $TiOSO_4$ as an electrolyte additive is an effective method to maintain the original EMD phase and suppress the formation of the Zn-containing phases with cycling. Energy-dispersive X-ray spectroscopy (EDX) indicates that a small amount of Ti is

---

Q. Duan, Y. Zheng, Y. Zhou, S. Dong, C. Ku, P. H.-L. Sit
School of Energy and Environment
City University of Hong Kong
83 Tat Chee Avenue, Kowloon, Hong Kong SAR China

D. Y. W. Yu
Research Center for Energy and Environmental Materials (GREEN)
National Institute for Materials Science
Namiki 1-1, Tsukuba, Ibaraki 305-0044, Japan
E-mail: yu.denis@nims.go.jp

The ORCID identification number(s) for the author(s) of this article can be found under https://doi.org/10.1002/smll.202404368

DOI: 10.1002/smll.202404368

incorporated into EMD during cycling while co-deposition of Zn and Mn is suppressed. Density functional theory (DFT) calculations confirm that it is less thermodynamically favorable for Zn to be incorporated into MnO_2 in the presence of Ti in the material. In addition, inductively-coupled plasma (ICP) spectroscopy results show that the changes in Mn^{2+} concentration in the electrolyte are reversible while electrochemical impedance spectroscopy (EIS) measurements reveal that cell resistance of MnO_2-Zn batteries is stable over cycling with $TiOSO_4$ additive. As a result, with 0.5 wt.% $TiOSO_4$ additive, MnO_2-Zn battery demonstrates a stable capacity of 230 mAh g^{-1} for over 1500 cycles under a current of 1200 mA g^{-1}, corresponding to a charge–discharge time of ≈12 min (5C rate). Stable cycling can be achieved at even higher current rates, with a capacity of 92 mAh g^{-1} at 4800 mA g^{-1} after 10 000 cycles.

2. Results and Discussion

2.1. Contributions to Capacity of MnO_2

Commercial EMD is selected as the active material in this study as they are readily available. The ball-milled material has a particle size of ~100 nm from scanning electron microscopy (SEM) and transmission electron microscopy (TEM) observations (Figure S1a,b, Supporting Information). Brunauer-Emmett-Teller (BET) surface area of the material is 57.3 m^2 g^{-1} after ballmill (Figure S1c, Supporting Information). The X-ray diffraction (XRD pattern of the commercial EMD is given in Figure S1d (Supporting Information), which shows that it has a crystalline phase of γ-MnO_2 (JCPDS #14-0644), a tunneled structure with an intergrowth of Pyrolusite and Ramsdellite phases with (1 × 1) and (2 × 1) tunnels of MnO_6 octahedral units, respectively (Figure S1e, Supporting Information). EDX analysis of the material shows that it contains Mn and O (Figure S1f, Supporting Information).

To investigate the structural changes in the electrode during charge–discharge, in situ XRD was conducted during first cycle (**Figure** 1a,b; Figure S2, Supporting Information). Before discharge, the pristine γ-MnO_2 peaks located at 16.7°, 19.2°, 24.9°, and 29.3° can be observed, together with the peak of the polytetrahluoroethylene (PTFE) binder at 8.2° and paraffin pouch bag at 9.7°. Along with discharge at 30 mA g^{-1}, all the γ-MnO_2 peaks shift to lower angles with an increase in lattice parameters, while the peaks shift back during charging. For example, the (160) crystal plane located at 24.9° has a linear increase in lattice space from 1.65 to 1.70 Å after fully discharge (Figure 1b). This behavior is consistent with the intercalation/de-intercalation of proton into the lattice, as previous works have shown that it is unlikely for Zn^{2+} to intercalate into MnO_2 tunnels.[8,27] We note that the shift of the EMD peaks is linear with time, suggesting that the proton reaction occurs evenly throughout the charge–discharge process. Meanwhile, invariant peaks at 7.5°, 11.3°, 15.2°, 15.9°, 22.5°, and 26.0°, etc. emerge after discharging for ≈3 h (60 mAh g^{-1}) and disappear in the middle of the charge process. These peaks are attributed to zinc hydroxide sulfate (ZHS, $Zn_4SO_4(OH)_6{\cdot}5H_2O$, JPCDS #39-0688), which is typically formed when the pH of the electrolyte is increased.[28] This confirms that there are proton-coupled reactions (PCRs) during the discharge–charge process.[29]

EMD electrodes were extracted from the batteries at different states of charge and observed by SEM to further investigate the emergence of the ZHS phase. In Figure 1c, the SEM image of the pristine MnO_2 electrode shows that the cathode is mainly composed of compact EMD particles. When the battery is discharged to 1.2 V, some flake-like products that are attributed to ZHS are observed on the electrode surface (Figure 1d). After the cell is fully discharged to 0.8 V, the electrode surface is completely covered by the flakes (Figure 1e). During the charge process, the flakes gradually disappear, and the original particle-like morphology is observed again (Figure 1f,g). The SEM results are consistent with the XRD data in Figure 1a.

Since there are two parallel charge–discharge processes, here, we further quantify the contribution from the Mn dissolution/deposition reactions by measuring the Mn^{2+} concentration in the electrolyte at different states of charge. The ICP results of the Mn^{2+} concentration during the first cycle (Figure 1h) are shown in Figure 1i. Since the electrolyte contains 0.1 M $MnSO_4$, the initial Mn^{2+} concentration is 100 mM. During initial discharge, the Mn^{2+} concentration increases linearly by around 30 mM, which indicates that Mn dissolution accounts for a capacity of 107.2 mAh g^{-1} (42.8% of the observed capacity) (see calculation method in Note S1, Supporting Information). When the MnO_2 electrode is charged, the Mn^{2+} content decreases, indicating that it is re-deposited onto the electrode. After the end of 1st charge (state G with a charge capacity of 244 mAh g^{-1}), the Mn^{2+} concentration drops back close to the initial value of 100 mM, indicating complete reversibility of the Mn dissolution/deposition process during the first cycle.

Meanwhile, the capacity contribution from H^+ (de)insertion is investigated by an electrolyte-swapping experiment. Specifically, an EMD electrode was initially fully discharged in 1 M $ZnSO_4$ + 0.1 M $MnSO_4$ (1Zn+0.1Mn) electrolyte. The cell was then disassembled and the EMD electrode was washed carefully with deionized water to remove the electrolyte, where the dissolved Mn^{2+} from discharge process is removed. The electrode was then reassembled with 1 M $ZnSO_4$ (1 Zn) electrolyte and charged. Since there is no Mn^{2+} in the electrolyte anymore after electrolyte swapping, the charge capacity can only come from proton desertion from the active material. Figure 1j shows that the charge profile of the cell with electrolyte-swapping is different from the usual charge curve in Figure 1h. In particular, a much smaller charge capacity of 145 mAh g^{-1}, corresponding to 59.2% of the discharge capacity is observed from the cell after electrolyte swapping.

Overall, the electrolyte-swapping and ICP tests complement each other and suggest that about 60% of the charge capacity of EMD comes from proton desertion and 40% comes from Mn deposition.

It is noteworthy that even though there is 0.1 MM $MnSO_4$ preadded into the electrolyte, there is still a significant amount of Mn dissolution that gives rise to the reversible capacity. This observation is contradictory to a common belief that the Mn^{2+} additive can suppress the Mn dissolution caused by Jahn–Teller effect.[7] In fact, considering the MnO_2-Zn system as a partial electrolytic Mn-Zn battery, the Mn^{2+} additive in the electrolyte can act as a Mn reservoir to promote the re-deposition of Mn^{2+}, thereby improving the reversibility of the MnO_2 dissolution/deposition reaction. The effect is more obvious in the case of an excess amount of electrolyte. Figure S3 (Supporting Information) shows

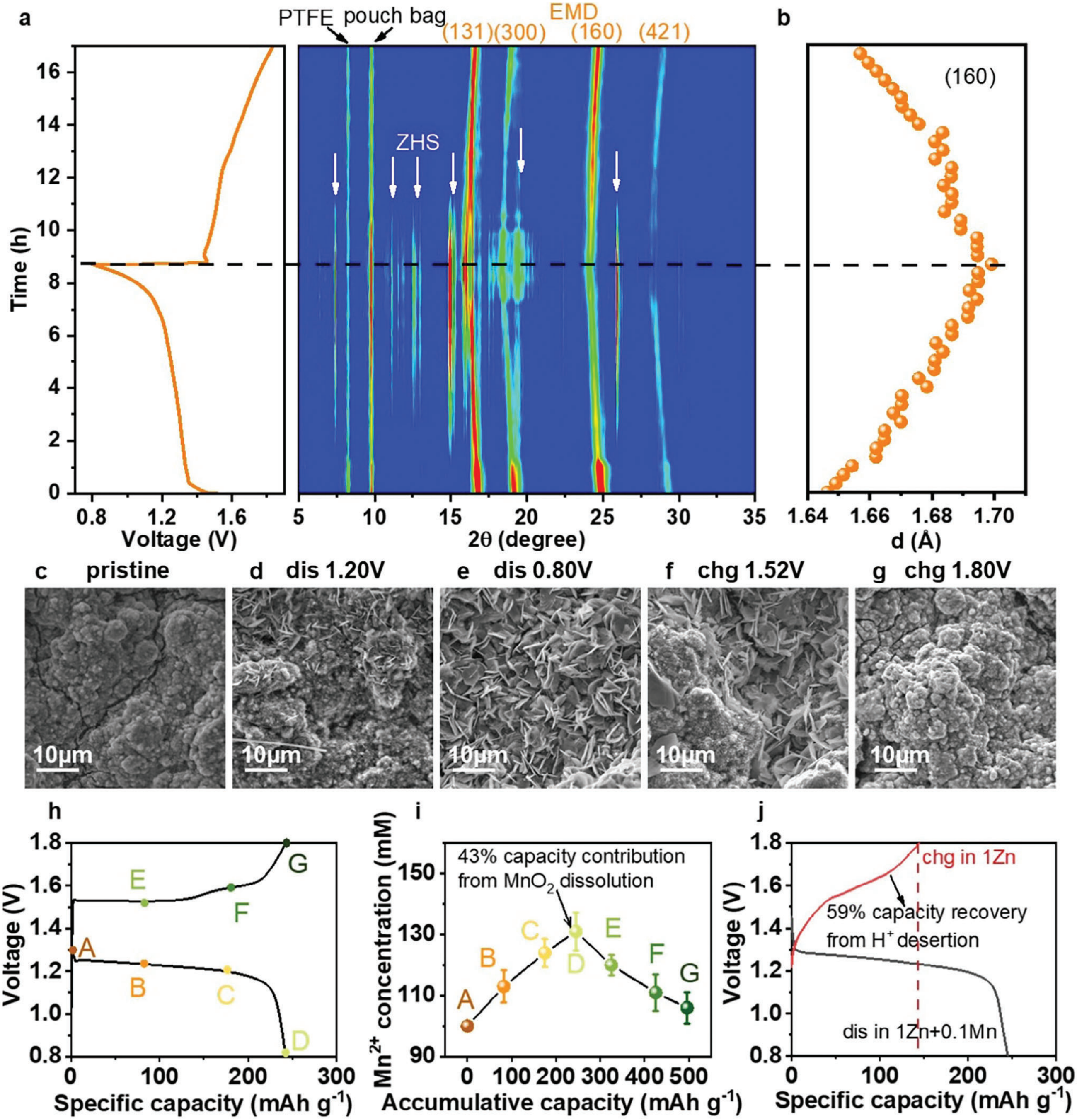

Figure 1. In situ XRD profiles of EMD electrode during the 1st cycle: a) full spectrum, b) lattice spacing of the (160) crystal plane of EMD; SEM images of EMD electrodes: c) pristine, d) discharge to 1.20 V, e) discharge to 0.80 V, f) charge to 1.52 V, g) charge to 1.80 V; h) voltage profile of the 1st cycle; i) concentration change of Mn^{2+} in the electrolyte from ICP; j) voltage profile of the electrolyte-swapping experiment.

the 1st cycle charge–discharge profile of MnO$_2$-Zn batteries in 1 M ZnSO$_4$ electrolyte with or without MnSO$_4$ additive in an electrolyte-lean coin cell (200 μL) and an electrolyte-rich beaker cell (5 mL) with the same amount of MnO$_2$ active material mass. For both cells with 1Zn+0.1Mn electrolyte (Figure S3b, Supporting Information), they show similar voltage profiles, capacity, and first cycle efficiency as there is ample Mn^{2+} in the electrolyte that can be re-deposited during charging. On the other hand, the electrode tested in a beaker cell with 1 Zn electrolyte exhibits a much lower charge capacity than that from a coin cell (Figure S3a, Supporting Information). Because of the larger amount of electrolyte in the beaker cell, the overall concentration of Mn^{2+} in the electrolyte after discharging is lower. The voltage polarization during charging is therefore larger and a smaller amount

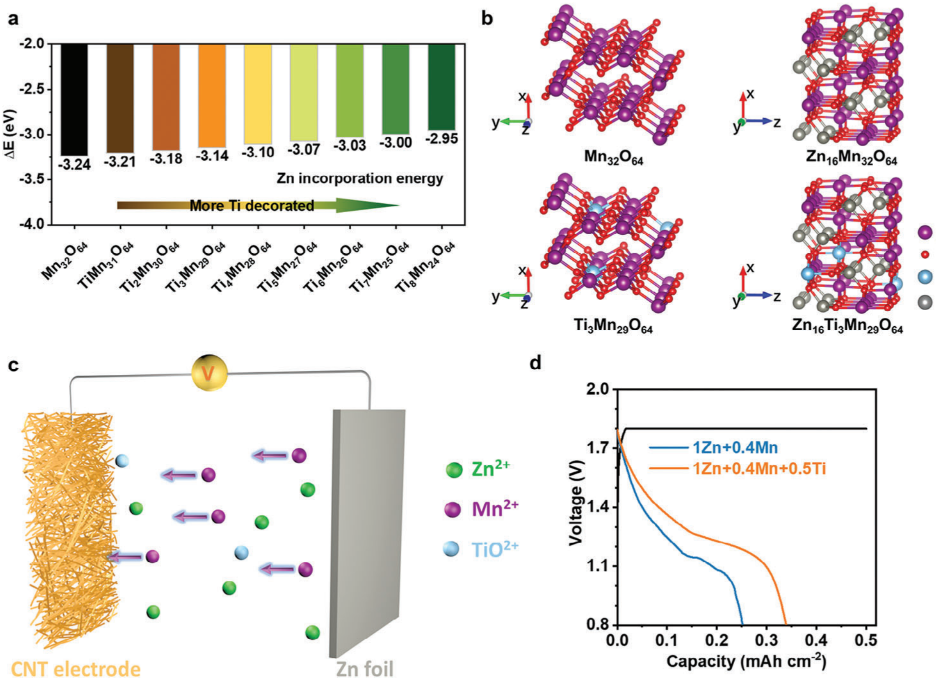

Figure 2. a) DFT calculation comparing the formation energy difference (ΔE) per Zn atom of Zn-incorporated EMD with different amount of Ti; b) molecular structures of EMD, EMD (with 3/32 Ti substitution), Zn-inserted EMD and Zn-inserted EMD with Ti in the calculation; c) schematic illustration of the electrodeposition test configuration; d) 1st cycle voltage profiles of the electrodeposition tests in 1Zn+0.4Mn and 1Zn+0.4Mn+0.5Ti electrolyte with a capacity limit of 0.5 mAh cm^{-2}.

of MnO_2 can be deposited back before the voltage reaches the upper cutoff. This observation is also consistent with previous studies.[30]

2.2. Effect of Ti and Zn on Mn Dissolution/Deposition Process

As the electrolyte in a MnO_2-Zn battery contains both Zn^{2+} and Mn^{2+} and Mn dissolution/deposition process accounts for a large part of the capacity, it is plausible that Zn ions can be co-deposited during charging to form Zn—Mn—O phases. To study the likelihood of it, here, we first conducted DFT simulations to calculate the formation energy difference (ΔE) of EMD (MnO_2) and $ZnMn_2O_4$. We found that $ZnMn_2O_4$ has a lower energy of 3.24 eV per Zn atom than MnO_2, indicating that it is more thermodynamically favorable for Zn to be incorporated into MnO_2 (**Figure** 2a,b).

To suppress the co-deposition of Zn and Mn, one would need to make it less favorable for Zn to enter the MnO_2 structure. Previous research works have shown that Ti-doping can improve the stability of MnO_2 in alkaline medium.[28,31] We therefore further study here whether the addition of Ti can also reduce the formation of Zn—Mn—O phases. First, we calculated how the difference in the formation energy between MnO_2 with Ti ($Ti_xMn_{32\text{-}x}O_{64}$) and the corresponding Zn-containing compound ($Zn_yTi_xMn_{32\text{-}x}O_{64}$) changes with Ti content by DFT. The results (Figure 2a,b) show that the energy gain from inserting Zn into MnO_2 with Ti is reduced with increasing Ti content, which suggests that the formation of Zn—Mn—O phases is less likely with Ti in the structure, compared to without.

Then, to prove the effect of Ti experimentally, we designed a MnO_2 electrodeposition test in electrolyte in the presence of Zn^{2+} with or without Ti, as illustrated in Figure 2c and characterized the deposited films. Specifically, a bare CNT film is used as the cathode using a 1 M $ZnSO_4$ + 0.4 M $MnSO_4$ (1Zn+0.4Mn) electrolyte with and without 0.5% $TiOSO_4$ additive. Note that the $MnSO_4$ content in the electrolyte is higher in the electrodeposition test compared to the battery test so as to facilitate Mn deposition, and $TiOSO_4$ that can be dissolved easily in water was used as the Ti source. During the constant voltage charge at 1.8 V, Mn^{2+} in the electrolyte is oxidized to EMD and deposited on the CNT substrate surface. The charge capacity is limited to 0.5 mAh cm^{-2}, which corresponds to the deposition of 0.81 mg cm^{-2} of MnO_2 assuming 2e$^-$ transfer.

After deposition (initial charge), the CNT electrodes were studied with XRD to investigate the structure of the deposited materials. The results in **Figure** 3a show that γ-MnO_2 similar to commercial EMD are mainly formed with or without $TiOSO_4$ additive.[32] For the sample deposited in 1Zn+0.4Mn electrolyte, small peaks attributed to $ZnMn_2O_4$ and $ZnMn_3O_7$ can also be observed,[13] which indicates that there are Zn-containing side-products from the EMD deposition, apart from the main reaction. On the other hand, the peaks of the EMD deposited in 1 M $ZnSO_4$ + 0.4 M $MnSO_4$ + 0.5 wt.% $TiOSO_4$ (1Zn+0.4Mn+0.5Ti) electrolyte are broader, which is attributed to the reduced crystallinity of the EMD with Ti, while no zinc-containing phases can be observed.

The electrodes were further studied with SEM and EDX to investigate the morphology and composition of the deposited EMDs. The deposited EMD in the 1Zn+0.4Mn electrolyte

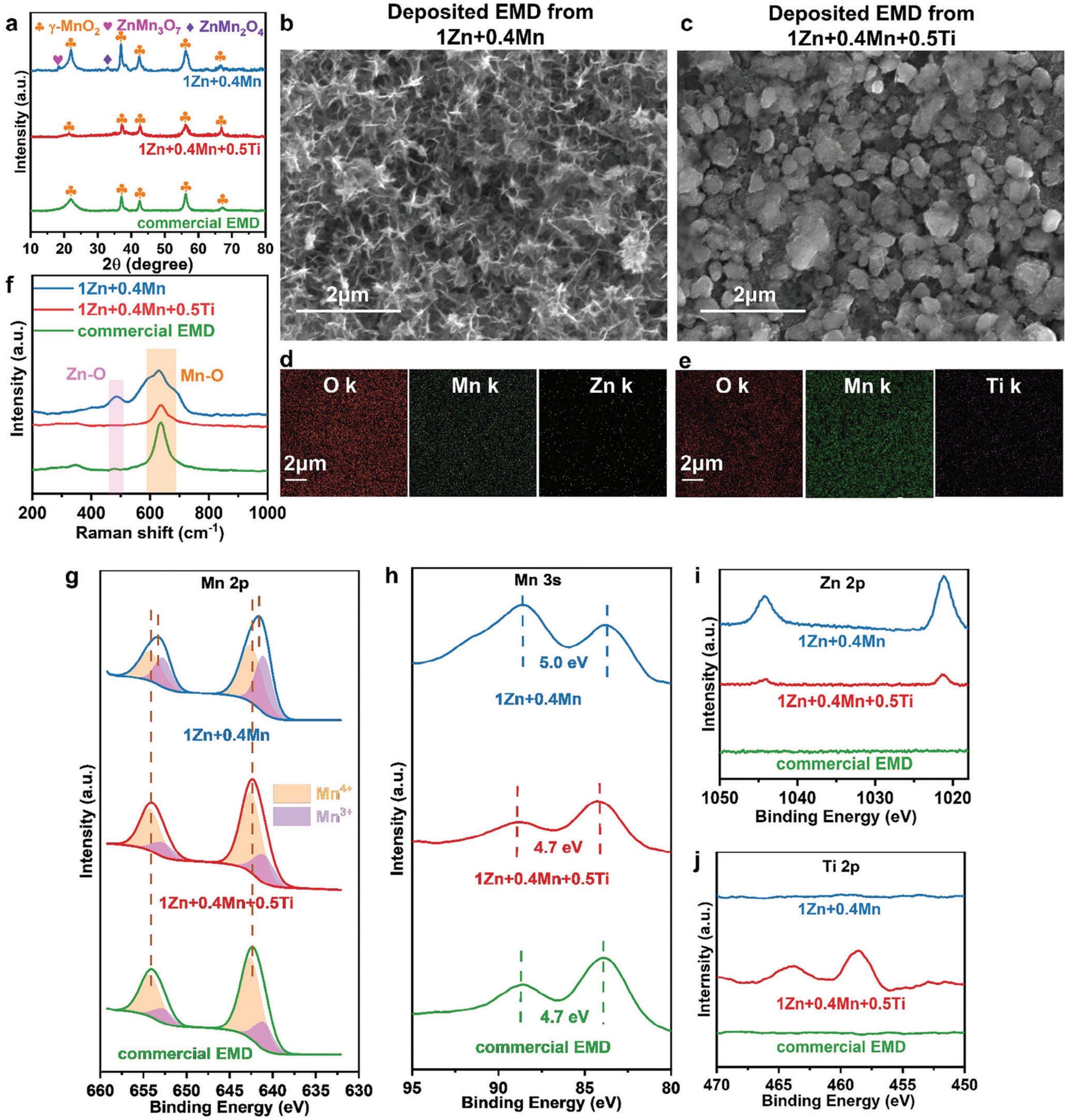

Figure 3. Characterizations of the electrodes after charging from the 1Zn+0.4Mn and 1Zn+0.4Mn+0.5Ti electrolyte in the electrodeposition tests: a) XRD patterns; SEM images of b) CNT electrode after charging in the 1Zn+0.4Mn electrolyte, c) CNT electrode after charging in the 1Zn+0.4Mn+0.5Ti electrolyte; d,e) elemental mapping images of (b,c), respectively; f) Raman spectra, g) XPS Mn 2p spectra, h) Mn 3s spectra, i) Zn 2p spectra, j) Ti 2p spectra of the two samples together with commercial EMD.

exhibits a flake-like structure (Figure 3b), while the one deposited in electrolyte with TiOSO$_4$ is particle-like (Figure 3c). EDX images (Figure 3d,e) show that the different elements are distributed uniformly in the deposited samples. For both samples, Mn and O are the main elements observed, indicating that the deposited product is mainly MnO$_2$. Though, the electrode deposited in 1Zn+0.4Mn electrolyte shows ≈5 at.% of Zn in it, while the one deposited in 1Zn+0.4Mn+0.5Ti electrolyte does not show any Zn signal, but instead about 3 at.% Ti (see Table S1, Supporting Information, for the specific atomic ratios). Since no S element is observed in both samples, SO$_4^{2-}$ ions do not participate during the deposition process, and so there is no residual electrolyte on the surface. The results indicate that there is a codeposition of Zn and Mn in 1Zn+0.4Mn electrolyte during the charge process. In comparison, in the presence of Ti in the electrolyte, Ti is preferably incorporated into EMD instead of Zn, consistent with the DFT calculations.

Raman spectra of the 2 electrodes were further taken, as shown in Figure 3f. The EMD deposited in the $TiOSO_4$-containing electrolyte exhibits only the Mn–O peak located at 636 cm^{-1} similar to that of commercial EMD,[33] while the electrode deposited in 1Zn+0.4Mn electrolyte contains an extra peak at 486 cm^{-1}, which can be attributed to the Zn–O peak in Zn_xMn_yO phases.[34]

The samples were also analyzed with X-ray photoelectron spectroscopy (XPS) to further investigate the Mn valence states. The Mn 2p spectra can be deconvoluted into Mn^{4+} and Mn^{3+} doublet peaks as shown in Figure 3g.[35] Comparing to the commercial EMD and the electrode deposited with $TiOSO_4$, the Mn 2p peaks of the electrode deposited in the 1Zn+0.4Mn electrolyte shift to a lower binding energy, suggesting the sample contains more Mn^{3+}. Moreover, the magnitude of Mn 3s peak splitting of the electrode in 1Zn+0.4Mn electrolyte is also increased compared to the other two samples (Figure 3h). As the magnitude of Mn 3s peak splitting depends on the Mn oxidation state because of the coupling of non-ionized 3s electron with 3d valence-band electrons, both Mn 2p and 3s spectra reveal that the Mn average oxidation state of the deposited EMD without Ti is lower.[36] This is consistent with the presence of $ZnMn_2O_4$ products as shown in the XRD analysis with a Mn valance of 3+. The codeposition of Zn with Mn is also verified as Zn 2p XPS peaks can be observed from the electrode (Figure 3i; Figure S4, Supporting Information).[37]

On the other hand, the deposited EMD from the $TiOSO_4$-contained electrolyte shows mainly XPS peaks corresponding to Mn^{4+}, which indicates that Ti not only suppresses the formation of Zn-containing products but also has little effect on Mn valence of the product. A small amount of Ti is incorporated into the deposited EMD, as Ti 2p XPS peaks can be observed in the electrode made with $TiOSO_4$ (Figure 3j; Figure S4, Supporting Information),[38] consistent with the EDX results (Table S1, Supporting Information).

Overall, the results indicate that EMD with Zn—Mn—O phases are formed during electrodeposition in the presence of Zn and Mn ions in the electrolyte. In contrast, only EMD phase with a small amount of Ti is detected when Ti ions are added to the electrolyte without Zn—Mn—O phases. It is unlikely that the Ti atoms exist in the form of TiO_2, as TiO_2 phases are not detected from the XRD nor Raman spectroscopy (Figure S5, Supporting Information) of the electrode.[39] Ti is also not likely to be in the tunnels of EMD, as the tunnel sizes are 2.3 Å × 2.3 Å and 2.3 Å × 4.6 Å, which are smaller than the typical Ti-O bonds of ≈3.7 Å.[40] Moreover, the Ti element in the structure is not ion-exchangeable. After immersing the electrode in 0.5 M $NaSO_4$ solution overnight, the electrode shows no Na signal while the Mn/Ti ratio remains the same from EDX measurements (Table S2, Supporting Information). It is therefore likely that Ti^{4+} is incorporated into the MnO_6 octahedral units of EMD, as Mn and Ti have similar size, charge, and coordination number, as illustrated in Figure S6 (Supporting Information).[41]

The reversibility of the electrodeposited EMD electrodes in the two electrolytes was also tested by discharging them to 0.8 V afterward. From the voltage profiles shown in Figure 2d, one can see that the electrode in 1Zn+0.4Mn+0.5Ti electrolyte exhibits a larger initial discharge capacity, as compared to that with the 1Zn+0.4Mn electrolyte. Similar behaviors are also observed with different areal capacity limits (Figure S7, Supporting Information). This indicates that the EMD deposited with $TiOSO_4$ additive is more reversible. Apart from the higher 1st cycle reversibility, EMD deposited in 1Zn+0.4Mn+0.5Ti electrolyte also shows improved cyclability (Figure S8, Supporting Information), which is attributed to the absence of zinc-containing phases in the material.

2.3. Electrochemical Performances of MnO_2 Electrodes with/without $TiOSO_4$ Electrolyte Additive

As shown in the previous section, Ti additive in the electrolyte facilitates the reversibility of Mn dissolution and deposition without the formation of zinc-containing phases. Here, we will explore how the $TiOSO_4$ additive affects the electrochemical performance of composite electrodes with MnO_2 powder. First, 1 Zn, 1Zn+0.1Mn or 1 M $ZnSO_4$ + 0.1 M $MnSO_4$ + 0.5 wt.% $TiOSO_4$ (1Zn+0.1Mn+0.5Ti) electrolytes were prepared and their ionic conductivity and pH are shown in Table S3 (Supporting Information). The ionic conductivities of them are about the same. Even though the pH of the electrolyte drops from 4.61 to 2.03 after $TiOSO_4$ addition, we demonstrated that this pH change is not responsible for the improved cycle stability of MnO_2, as the cycle performance of the EMD is poor in an electrolyte with pH 2.1 without Ti (Figure S9, Supporting Information). EMD-Zn cells with the different electrolytes were then subjected to cyclic voltammetry (CV) tests. The results in **Figure 4a** show that all the cells exhibit two distinctive redox peaks that are originated from the charge–discharge reactions of EMD, as negligible capacity is obtained from a bare Ketjen black (KB) cathode without EMD (Figure S10, Supporting Information). So MnO_2 undergoes the same charge–discharge mechanisms (i.e., proton (de)insertion and Mn dissolution/deposition processes) initially in all three electrolytes with or without Ti additive.

To test the cycle stability of the EMD electrode with different electrolytes, they were first charged and discharged at a current of 1200 mA g^{-1} (about 5C). The results are shown in Figure 4b. While EMD tested in $ZnSO_4$ electrolyte shows a fast capacity decay, the cell with 1Zn+0.1Mn electrolyte exhibits a better cycle stability with a slower capacity fading, indicating Mn addition can improve reversibility, in line with the observations of many other literatures.[7] However, the capacity still suddenly drops after about 200 cycles. In comparison, the cell tested with 1Zn+0.1Mn+0.5Ti electrolyte shows significant improvement in cyclability. After 1500 cycles, it still exhibits a capacity of 230 mAh g^{-1}, corresponding to a capacity retention of ≈100% comparing to the initial cycle capacity. The voltage profiles of the three cells at different cycle numbers are shown in Figure 4d–f. Different from the drastic decay in capacity for the cells in 1 Zn and 1Zn+0.1Mn electrolytes, that tested in 1Zn+0.1Mn+0.5Ti electrolyte exhibits overlapping discharge–charge curves over 1500 cycles. This indicates that during cycling, the charge–discharge mechanism of EMD in 1 Zn and 1Zn+0.1Mn electrolytes is changed, while that tested in 1Zn+0.1Mn+0.5Ti remains the

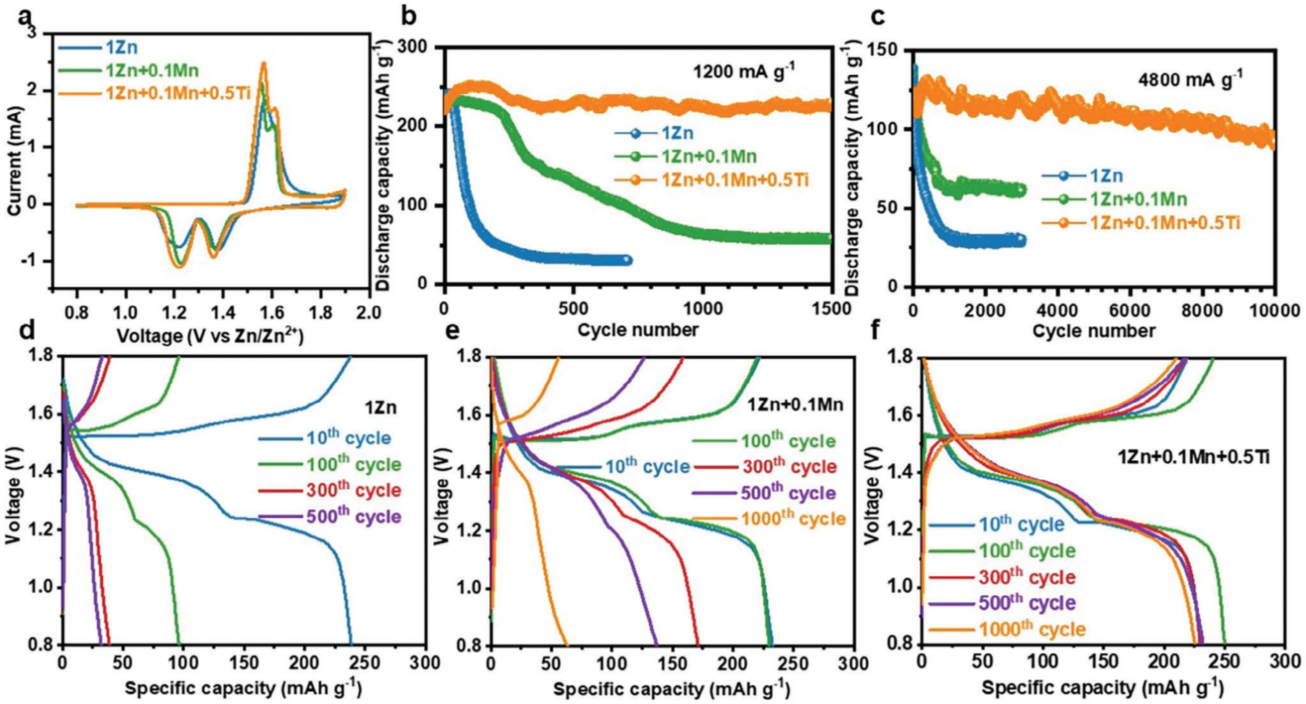

Figure 4. Electrochemical tests of the cell using 1 Zn, 1Zn+0.1Mn, 1Zn+0.1Mn+0.5Ti electrolyte: a) CV curves; b) cycle stability at 1200 mA g^{-1}; c) cycle stability at 4800 mA g^{-1}; voltage profiles of cells with d) 1 Zn electrolyte, e) 1Zn+0.1Mn electrolyte, f) 1Zn+0.1Mn+0.5Ti electrolyte.

same throughout. In addition, the cycle stability of EMD electrode with $TiOSO_4$ electrolyte additive is improved also under different current densities. As displayed in Figure 4c, the cell with 1Zn+0.1Mn+0.5Ti electrolyte can still obtain a capacity of 92 mAh g^{-1} after 10 000 cycles under 4800 mA g^{-1}, superior to those of the cell with 1Zn+0.1Mn electrolyte (60 mAh g^{-1} after 3000 cycles at 4800 mA g^{-1}). The cycling performance is also the best amongst recently reported MnO_2-Zn batteries, as summarized in Table S4 (Supporting Information).[12,14,21,24,42–46] The superior cycle performance of EMD in 1Zn+0.1Mn+0.5Ti electrolyte is also observed at a low current rate of 300 mA g^{-1} (about 1C) where 90% capacity is maintained after 400 cycles (Figure S11, Supporting Information). In comparison, drastic capacity fading is observed in cells tested in electrolyte without Ti.

2.4. The role of Ti Additive Toward the Stability of EMD-Zn Batteries

To understand why Ti additive is able to improve cycle stability, we charged/discharged the EMD-Zn batteries in 1Zn+0.1Mn and 1Zn+0.1Mn+0.5Ti electrolytes to different number of cycles and extracted the electrolytes and the EMD cathodes from them for XRD studies. For the MnO_2 electrode tested in 1Zn+0.1Mn (**Figure 5a**), after 5 cycles, the original EMD peaks can hardly be seen, while weak XRD peaks located at 32.9° and 36.4° corresponding to $ZnMn_2O_4$ (JPCDS#24-1133) are observed.[47] After 300 cycles, the characteristic XRD peak of $ZnMn_3O_7$ (JPCDS#47-1825) shows up at 18.5°.[48] We can find that these Zn-containing phases exist under both the discharge and charge states after 300 cycles, which indicates their irreversibility. Note that during initial cycle from in situ XRD (Figure 1a), the Zn—Mn—O phases can hardly be seen because their amount is small. With cycling (i.e., 5th, 300th, and 500th XRD profiles in Figure 5a), one can see that their X-ray peak intensities continue to grow, showing that these phases accumulate with repeated charge–discharge. Even though the emerged Zn—Mn—O phases such as $ZnMn_2O_4$ can be charged and discharged, as shown from an electrochemical test of as-synthesized $ZnMn_2O_4$ electrode in Figure S12 (Supporting Information) as an example, they give a much smaller capacity than the original MnO_2. Thus, the reduction in capacity of EMD in $ZnSO_4$ and $MnSO_4$ containing electrolyte can be attributed to the formation of Zn—Mn—O phases with cycling, which consumes the active Mn in the electrolyte.

In comparison, the XRD patterns of the EMD cathodes cycled with 1Zn+0.1Mn+0.5Ti electrolyte show different behaviors (Figure 5b). Specifically, EMD peaks and ZHS peaks as observed at the charged and discharged states, respectively, are well maintained for 500 cycles, and Zn-containing phases can hardly be observed. In addition, SEM observations of the electrode tested in 1Zn+0.1Mn electrolyte (Figure 5c) show nanoflakes on its surface, similar to that reported in previous literature,[47] while that tested in 1Zn+0.1Mn+0.5Ti electrolyte (Figure 5d) exhibit a nano particle morphology, in line with the observed morphologies of our electrodeposited material in Figure 3b,c. Moreover, high resolution transmission electron microscopy (HRTEM) images of the electrode tested with 1Zn+0.1Mn electrolyte (Figure 5c) show lattice fringes that are attributed to (002) from $ZnMn_3O_7$ and (211) from $ZnMn_2O_4$, which are consistent with the XRD peaks located at 18.5° and 36.4° in Figure 5a, while those from electrode

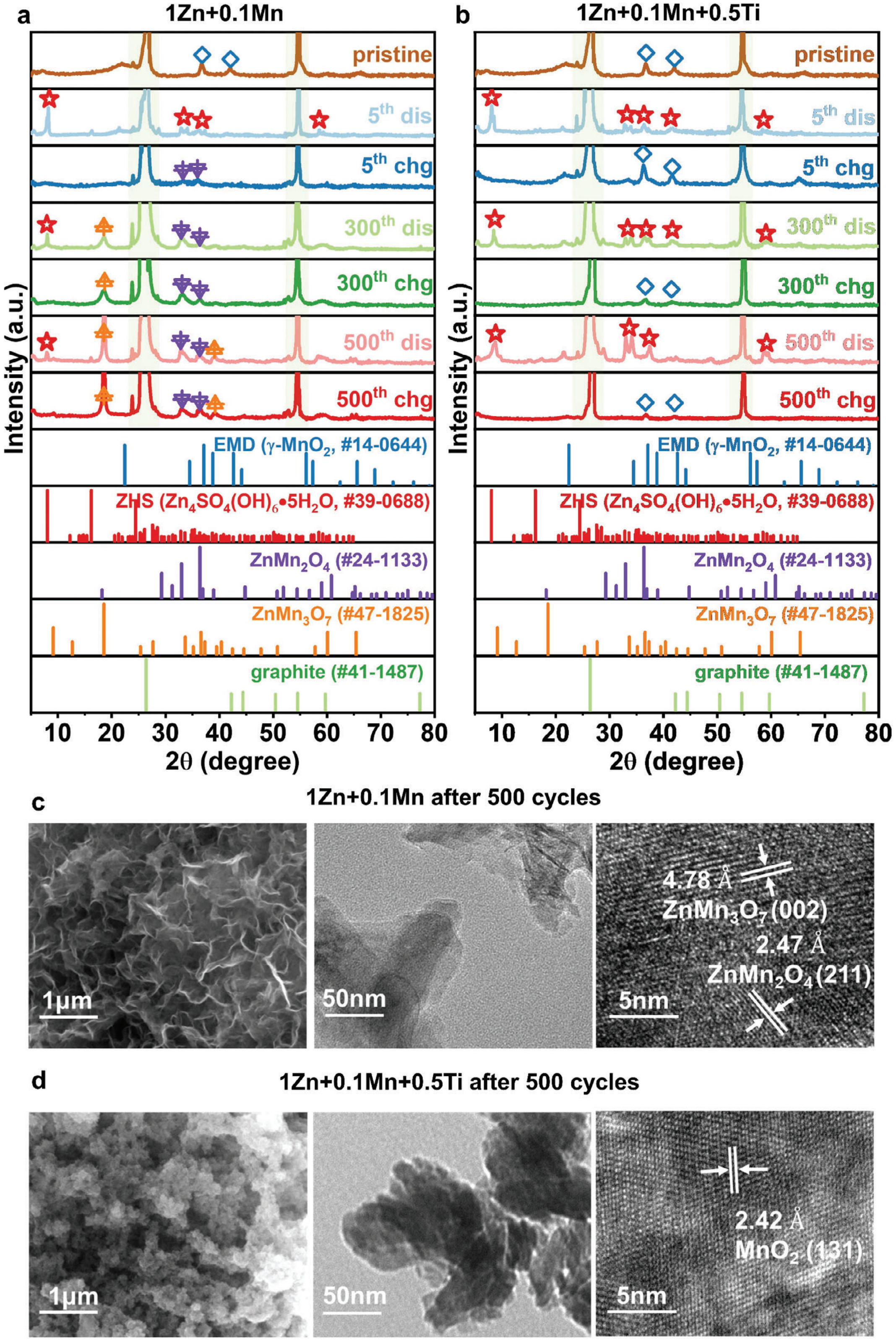

Figure 5. XRD patterns of the EMD cathode tested along cycling with a) 1Zn+0.1Mn electrolyte, b) with 1Zn+0.1Mn+0.5Ti electrolyte; SEM, TEM and HRTEM images of the cathodes in the c) 1Zn+0.1Mn electrolyte, d) 1Zn+0.1Mn+0.5Ti electrolyte after cycling for 500 cycles.

tested with Ti-containing electrolyte (Figure 5d) only show long-range (131) lattice fringe of EMD. All the above results clearly demonstrate that $TiOSO_4$ addition suppresses the formation of Zn-containing phases and improves the reversibility of EMD.

We also systematically monitored the changes in the Mn^{2+} concentration of the electrolytes over cycles via ICP analysis to better reveal the effect of Ti to the Mn dissolution/deposition process and the electrochemical performance of EMD. In general, we observed that the Mn^{2+} concentration rises during discharging due to Mn dissolution while it falls during charging due to Mn deposition. Though, the overall amount of Mn^{2+} in the electrolyte can change with cycling. As shown in **Figure 6a**, in a cell tested with 1 Zn electrolyte without any additive, Mn^{2+} content in the electrolyte increases within the initial 100 cycles, indicating there is more Mn dissolution than Mn deposition. This is likely because there is no Mn^{2+} in the electrolyte at the beginning, so some of the dissolved Mn^{2+} stays in the electrolyte with cycling. After 100 cycles, the Mn^{2+} concentrations of both discharged and charged states start to decline owing to the consumption of Mn^{2+} from the irreversible formation of Zn-containing Mn oxide species.

The addition of 0.1 M $MnSO_4$ into the electrolyte changes the overall trend of Mn^{2+} with cycling (Figure 6b). The Mn^{2+} concentration rises and falls during discharge and charge, respectively, and the value remains around 0.1 M during the initial cycles, indicating that the Mn^{2+} additive can effectively facilitate the re-deposition of Mn^{2+}. Though, with further cycling, an irreversible consumption of Mn^{2+} occurs where Mn^{2+} content continues to decrease, which is attributed to the formation of Zn—Mn—O phases. It is noteworthy that the drastic decrease in Mn^{2+} content after 300 cycles coincides with the abrupt capacity drop of the material in Figure 4b. In contrast, with $TiOSO_4$ additive, the normal rise and fall in Mn^{2+} concentration during each cycle remains stable even after 500 cycles (Figure 6c). Mn dissolution and deposition are reversible and there is no side reaction that consumes Mn with cycle. This confirms that $TiOSO_4$ additive is effective in suppressing the deposition of Zn-Mn oxides.

We further study how the electrolyte affects the impedance of the EMD-Zn with EIS measurements. The Nyquist plots of EMD-Zn cells with different electrolytes at the charged state after different number of cycles are displayed in Figure 6d–f. The EIS profiles exhibit two semi-circles, which can be assigned to interface resistance R_i and charge transfer resistance R_{ct} from higher to lower frequency, respectively. For all the three cells, the semi-circle representing R_{ct} increases with cycle number. The values of R_{ct} are obtained by fitting the curves with an equivalent circuit shown in Figure 6g and the results are shown in Figure 6h. Both cells tested with 1 Zn and 1Zn+0.1Mn electrolytes exhibit drastic increase in R_{ct} to about 300 Ω after 500 cycles. In contrast, the R_{ct} of the cell tested in 1Zn+0.1Mn+0.5Ti electrolyte only grows slightly to 57 Ω after 500 cycles. This indicates that $TiOSO_4$ addition can suppress impedance growth of the electrode. Based on our previous discussion, the growing R_{ct} can be ascribed to the formation of Zn-Mn oxides on the electrode which hinders the ion diffusion, and $TiOSO_4$ can impede such reaction.

The rate performances of EMD electrodes in different electrolytes were investigated, as shown in Figure 6i. One can see that the addition of $MnSO_4$ additive into the electrolyte can enhance the rate performance of EMD. This is attributed to the improved kinetic of the re-deposition of Mn^{2+} during the charge process with higher content of Mn^{2+} in the electrolyte. Further addition of $TiOSO_4$ into the electrolyte does not have a significant effect on the rate performance of the electrode. Specifically, the EMD electrode tested with 1Zn+0.1Mn+0.5Ti electrolyte shows a capacity of 302, 275, 250, 212, 165, 136, and 118 mAh g^{-1} at a current rate of 300, 600, 1200, 2400, 3600, 4800, and 6000 mA g^{-1}.

Overall, the power and energy that can be obtained from EMD-Zn cells with 1Zn+0.1Mn+0.5Ti electrolyte are plotted in the Ragone plot in Figure 6j. The battery can deliver an energy density of 390 Wh kg^{-1} at a power density of 390 W kg^{-1} (calculated based on the mass of cathode active material), and still holds an energy density of 153 Wh kg^{-1} when the power density is increased to 7800 W kg^{-1}, which is superior to most of the previously reported ZIBs.[12,14,21,24,42–44] Stability of EMD in fact depends on the amount of $TiOSO_4$ additive. Figure S13 (Supporting Information) shows the cycle performance of EMD in 1Zn+0.1Mn electrolyte with different amounts of $TiOSO_4$. One can see that the addition of 0.2 wt.% $TiOSO_4$ can already improve cycle stability, but it is not sufficient. Too much $TiOSO_4$ on the other hand reduces the overall capacity. 0.5 wt.% is the optimal amount that gives a good balance between stability and capacity.

We have seen that the addition of Ti into the electrolyte results in a Ti-decorated MnO_2 after charge–discharge, which improves the stability of the active material. A schematic illustration of such in situ Ti-decoration strategy is shown in **Figure 7**. One question that arises is whether a pre-doped MnO_2 with Ti (Ti-MnO_2) can also be cycled stably. To find out, we synthesized a pre-doped MnO_2 material with 2 at.% Ti by a precipitation method between a solution with 3.55 g $MnSO_4$, 6 mL of concentrated nitric acid with $TiOSO_4$ in 100 mL distilled water with another solution with 0.07 M $KMnO_4$ in 100 mL distilled water at 90 degrees. The synthesized Ti-MnO_2 material was made into electrodes and tested with 1 Zn electrolyte (Figure S14, Supporting Information). The result shows that the pre-doped MnO_2 with Ti still shows a decrease in capacity with cycling, compared to the in situ Ti-decorated EMD. This is probably because for the pre-doped MnO_2, Mn, and Ti are dissolved into the electrolyte during discharging, and the concentration of Ti in the electrolyte is too low for it to be re-deposited upon charging. Thus, in situ Ti-decoration is a more effective way to stabilize MnO_2. In addition, the $TiOSO_4$ additive can also improve the cycle stability of the other MnO_2 polymorphs like β-MnO_2, δ-MnO_2 and synthesized γ-MnO_2 (Figure S15, Supporting Information).

3. Conclusion

In this work, through systematic investigations of the EMD electrode and electrolyte, we verified the proton insertion and Mn dissolution-deposition reaction both contribute to the observed capacity in mild acidic aqueous MnO_2-Zn battery. It is found that the co-deposition of Zn^{2+} and Mn^{2+} during the charge process will irreversibly transform the original EMD phase into Zn-Mn oxides during cycling, and because the Zn-Mn oxides have much lower capacity than EMD, the overall capacity of the active material decays. By adding Mn^{2+} additive into the electrolyte at the beginning, reversibility of the Mn dissolution-deposition reaction can be improved but the Zn—Mn—O phase formation still impairs the cyclability of EMD upon cycling. Here, we show that $TiOSO_4$ as an electrolyte additive facilitates the in situ

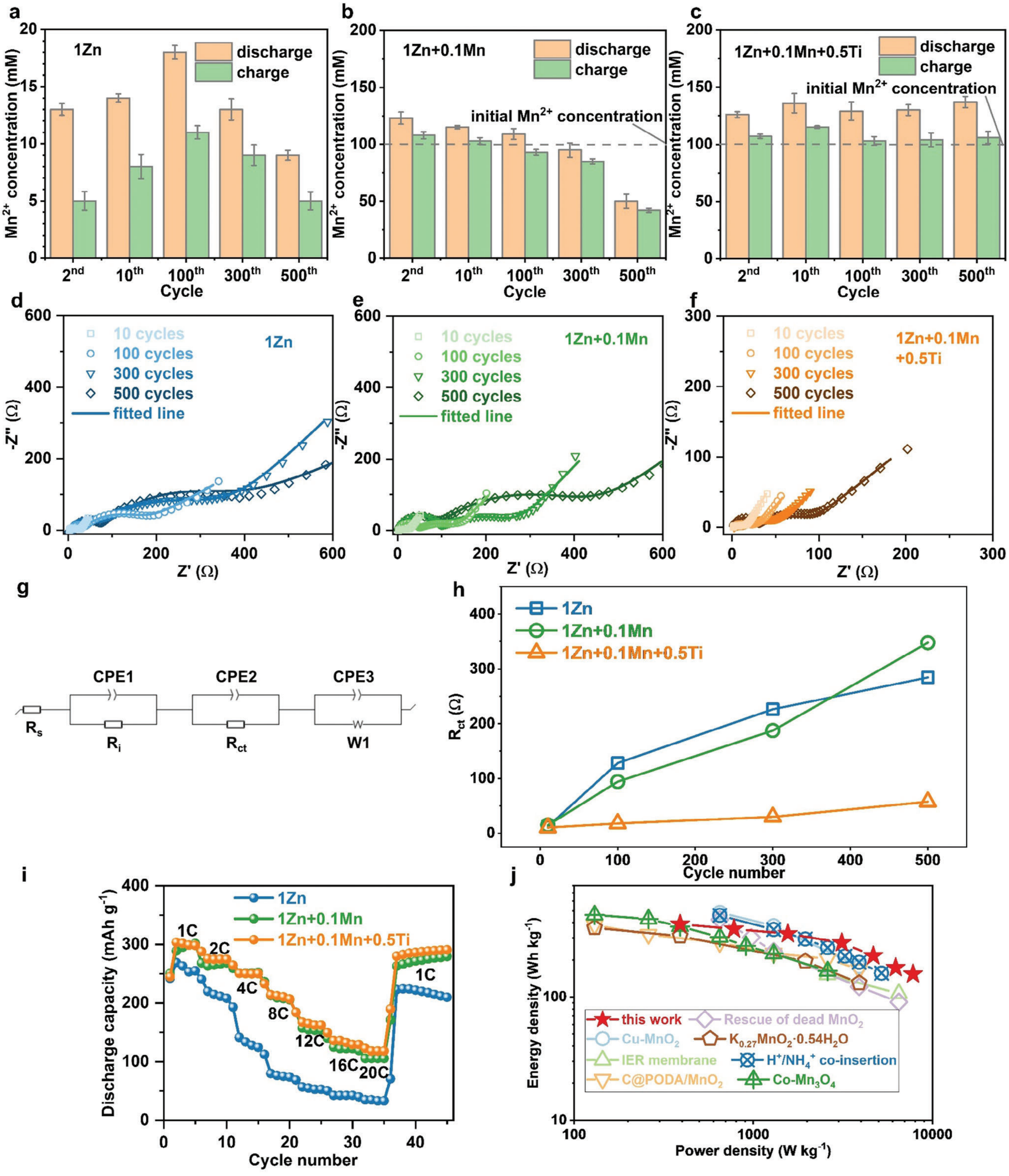

Figure 6. Mn^{2+} concentration in the electrolyte of the cell with a) 1 Zn, b) 1Zn+0.1Mn, c) 1Zn+0.1Mn+0.5Ti along cycling; Nyquist plots of the EIS results of the cell with d) 1 Zn, e) 1Zn+0.1Mn, f) 1Zn+0.1Mn+0.5Ti along cycling; g) equivalent circuit for EIS fitting; h) R_{ct} comparison of the cells over cycles from the EIS results; i) rate performance; j) energy and power density comparison with the recent works.

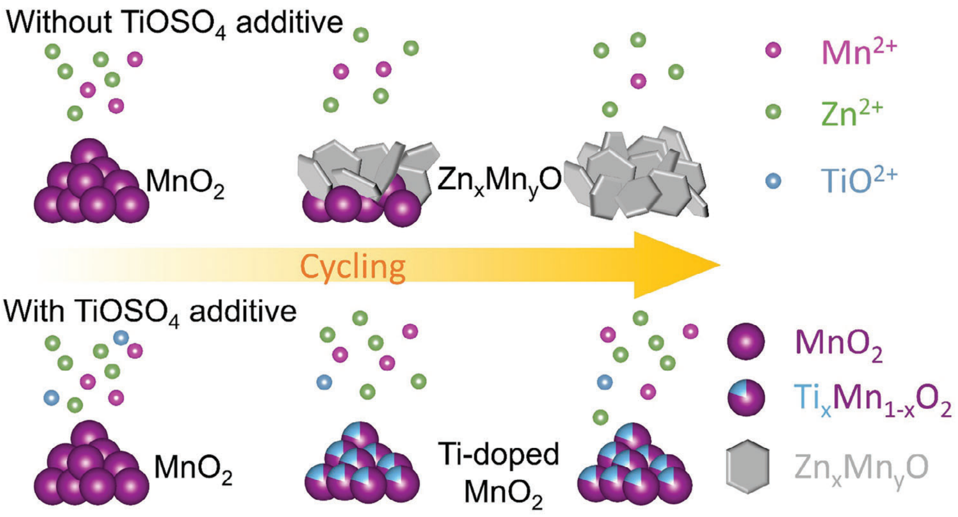

Figure 7. Schematic illustration of the effect of $TiOSO_4$ additive.

formation of a Ti-decorated EMD, which can suppress the formation of the Zn-Mn oxide species and significantly improve the cycle stability, as demonstrated through an electrodeposition test and other characterizations such as XPS, Raman, XRD, DFT calculations, etc. As a result, the EMD-Zn cell using 1Zn+0.1Mn+0.5Ti electrolyte achieves a remarkable cycle stability. Overall, our work provides fundamental insights into the battery mechanism with a strategy for improving the stability of EMD, which paves way for the further development of the mild acidic aqueous MnO_2-Zn batteries.

4. Experimental Section

Electrolyte Preparation and Cell Assembly: $ZnSO_4{\cdot}H_2O$ (>99.9%), $MnSO_4{\cdot}H_2O$ (>99%) and titanium oxysulfate $TiOSO_4$ (>29% Ti basis) were purchased from Sigma–Aldrich. The 1 M $ZnSO_4$ electrolyte was denoted as “1Zn”. The $ZnSO_4$ + $MnSO_4$ electrolyte was prepared through dissolving 1 Mм $ZnSO_4$ and 0.1 M $MnSO_4$ in de-ionized water, denoted as “1Zn+0.1Mn” for MnO_2-Zn battery testing; or 1 M $ZnSO_4$ and 0.4 M $MnSO_4$, denoted as “1Zn+0.4Mn” for the electrodeposition tests with CNT. The “1Zn+0.1Mn+0.5Ti” and “1Zn+0.4Mn+0.5Ti” electrolytes were prepared through dissolving 0.5 wt.% $TiOSO_4$ in the $ZnSO_4$ + $MnSO_4$ electrolytes. Electrolytes with other $TiOSO_4$ contents were prepared with the same method. All the electrolytes were prepared by stirring the electrolyte salts in water for more than 1 h at room temperature.

For making the EMD electrode, commercial EMD (Xiangtan Electrochemical Scientific Ltd.) was first ball-milled in zirconium oxide bowls at 200 rpm for 12 h with ethanol as the dispersant (EMD: ethanol = 1:1 in mass) to reduce the particle size. The resultant powder was dried at 60 °C for 4 h under vacuum to evaporate the ethanol. The ball-milled EMD was well mixed with Ketjen Black (KB-EC600JD) and polyvinylidene fluoride (PVdF, solef 5130, Solvay) in N-methyl-2-pyrrolidone (NMP) with a ratio of 7:2:1 to make a homogeneous slurry, which was coated on graphite paper (GP, 50 µm thick, Chenxin-Induction). The electrodes were punched out into a disc with a diameter of 16 mm and dried at 80 °C for 4 h. The typical EMD mass loading was ≈1.5 mg cm^{-2}. 2032 coin cells were assembled using the as-described electrode as cathode, zinc foil (Sigma–Aldrich, 99.9%, 50 µm thick) as anode, and glass fiber (Advantec #GD-120) as separator with 200 µl electrolyte. For the electrodeposition tests, a CNT sheet was used as the cathode. To prepare the cathode substrate, single-wall carbon nanotube dispersion (SWCNT, 13 wt.% in water, Jiacai Technology Co., Ltd.) was diluted 20 times with de-ionized water and stirred for 2 h at 70 °C. Then, the solution was filtered through a hydrophilic PTFE membrane by vacuum filtration to generate the free-standing CNT electrode with a thickness of about 10 µm. The CNT electrode was then coupled with Zn anode and made into a coin cell, similar to the MnO_2-Zn batteries.

To study the activity of the Zn—Mn—O phases, $ZnMn_2O_4$ was synthesized by a traditional sol-gel method based on a previous work.[49] Specifically, zinc acetate, manganese acetate and citric acid were mixed in molar ratio of 1:2:3.1 in de-ionized water, of which pH was adjusted to 6.8 with ammonium hydroxide. The solution was dried at 80 °C to form a gel and further annealed at 500 °C for 5 h to obtain the $ZnMn_2O_4$ powder.

Electrochemical Tests: Galvanostatic charge–discharge tests were performed using a Neware battery tester between 0.8 and 1.8 V. Cyclic voltammetry (CV, scanning rate 0.1 mV s^{-1}) and electrochemical impedance spectroscopy (EIS, frequency range 1 MHz–0.01 Hz) measurements were performed on a Bio-logic potentiostat (VMP3). For the electrodeposition tests, the cell was first charged with a constant current of 0.05 mA cm^{-2} to 1.8 V followed by a constant voltage step until the areal capacity reached 0.5 mAh cm^{-2}, and then discharged to 0.8 V with 0.05 mA cm^{-2}.

Characterizations: The morphological evolutions of the electrodes were characterized by scanning electron microscopy (SEM, QUATTROS), EDX, and transmission electron microscopy (TEM, JEOL 2100 F). X-ray photoelectron spectroscopy (XPS, Thermo Scientific Escalab), ex situ XRD (PANalytical X'Pert3 X-ray diffractometer with a Cu source), and Raman spectroscopy (WITec RAMAN alpha 300R @ R7167 BOC) were used to study the crystal structure changes of the electrodes. Nitrogen adsorption tests at 77 K using Micromeritics 3Flex was applied to obtain the Brunauer–Emmett–Teller (BET) surface area. Inductively-coupled plasma atomic emission spectroscopy (ICP-AES) was used to detect the Mn^{2+} ion concentrations in the electrolytes, and each data point was measured three times. To prepare the electrolyte samples for ICP, all parts from a disassembled coin cell were soaked in 20 mL de-ionized water and stirred overnight before sampling. For in situ XRD tests (Mo K_α source), a thick electrode (≈10 mg cm^{-2}) was made by mixing EMD, KB, and polytetrafluoroethylene (PTFE, DAIKIN) in a ratio of 7:2:1, and the resulting film was pressed on a stainless steel mesh. The experiment was conducted in transmission mode with a pouch cell consisting of the EMD electrode, 1Zn + 0.1Mn electrolyte, and a Zn foil with a hole to eliminate the X-ray signals from the anode.

Density Functional Theory Calculations: Density Functional Theory (DFT) calculations were performed using the Quantum Espresso package.[50,51] The ultrasoft GBRV pseudopotentials[52] were used with the PBE[53] exchange correlation functionals. The wavefunction and augmented charge density cutoffs were set to 40 Ry and 280 Ry, respectively.

PBE+U corrections were introduced to the Mn atoms with a U value of 4 eV.[12] Γ-point sampling was used for both the MnO_2 and $ZnMn_2O_4$ systems with lattice parameters obtained from the XRD tests mentioned earlier. For the case of MnO_2, the lattice parameters obtained from XRD matches the Ramsdellite phase. As a result, a $Mn_{32}O_{64}$ orthorhombic simulation cell with lattice parameters of $8.18\ \text{Å} \times 10.15\ \text{Å} \times 12.72\ \text{Å}$ was used. For the $ZnMn_2O_4$ system, a $Zn_{16}Mn_{32}O_{64}$ tetragonal simulation cell with lattice parameters of $11.44\ \text{Å} \times 11.44\ \text{Å} \times 9.25\ \text{Å}$ was used. Starting from the pristine MnO_2 and $ZnMn_2O_4$ systems, the Ti-decorated MnO_2 and $ZnMn_2O_4$ systems were generated by successively replacing randomly chosen Mn atoms with Ti atoms. Finally, a $2 \times 2 \times 2$ hexagonal supercell with lattice parameters of $5.33\ \text{Å} \times 5.33\ \text{Å} \times 9.89\ \text{Å}$[54] and $8 \times 8 \times 8$ k-point sampling was used for the Zn metal system with 16 Zn atoms per simulation cell.

Supporting Information

Supporting Information is available from the Wiley Online Library or from the author.

Acknowledgements

This study was supported by a Research Matching Grant Scheme (PJ9229008) by the government of Hong Kong Special Administrative Region.

Conflict of Interest

The authors declare no conflict of interest.

Data Availability Statement

The data that support the findings of this study are available from the corresponding author upon reasonable request.

Keywords

aqueous zinc-ion batteries, electrolyte additive, manganese dioxide, phase formation

Received: June 4, 2024
Revised: July 3, 2024
Published online:

---

[1] B. Tang, L. Shan, S. Liang, J. Zhou, *Energy Environ. Sci.* **2019**, *12*, 3288.
[2] C. Li, S. Jin, L. A. Archer, L. F. Nazar, *Joule* **2022**, *6*, 1733.
[3] Y. Liang, H. Dong, D. Aurbach, Y. Yao, *Nat. Energy* **2020**, *5*, 646.
[4] N. Zhang, X. Chen, M. Yu, Z. Niu, F. Cheng, J. Chen, *Chem. Soc. Rev.* **2020**, *49*, 4203.
[5] V. Mathew, B. Sambandam, S. Kim, S. Kim, S. Park, S. Lee, M. H. Alfaruqi, V. Soundharrajan, S. Islam, D. Yunianto Putro, J.-Y. Hwang, Y.-K. Sun, J. Kim, *ACS Energy Lett.* **2020**, *5*, 2376.
[6] N. Zhang, F. Cheng, J. Liu, L. Wang, X. Long, X. Liu, F. Li, J. Chen, *Nat. Commun.* **2017**, *8*, 405.
[7] H. Pan, Y. Shao, P. Yan, Y. Cheng, K. S. Han, Z. Nie, C. Wang, J. Yang, X. Li, P. Bhattacharya, K. T. Mueller, J. Liu, *Nat. Energy* **2016**, *1*, 16039.
[8] Y. Yuan, R. Sharpe, K. He, C. Li, M. T. Saray, T. Liu, W. Yao, M. Cheng, H. Jin, S. Wang, K. Amine, R. Shahbazian-Yassar, M. Saiful Islam, J. Lu, *Nat. Sustain.* **2022**, *5*, 890.
[9] L. Godeffroy, I. Aguilar, J. Médard, D. Larcher, J. Tarascon, F. Kanoufi, *Adv. Energy Mater.* **2022**, *12*, 2200722.
[10] Y. Li, S. Wang, J. R. Salvador, J. Wu, B. Liu, W. Yang, J. Yang, W. Zhang, J. Liu, J. Yang, *Chem. Mater.* **2019**, *31*, 2036.
[11] N. Becknell, P. P. Lopes, T. Hatsukade, X. Zhou, Y. Liu, B. Fisher, D. Y. Chung, M. G. Kanatzidis, N. M. Markovic, S. Tepavcevic, V. R. Stamenkovic, *Adv. Funct. Mater.* **2021**, *31*, 2102135.
[12] H. Yang, W. Zhou, D. Chen, J. Liu, Z. Yuan, M. Lu, L. Shen, V. Shulga, W. Han, D. Chao, *Energy Environ. Sci.* **2022**, *15*, 1106.
[13] S. Ding, L. Liu, R. Qin, X. Chen, A. Song, J. Li, S. Li, Q. Zhao, F. Pan, *ACS Appl. Mater. Interfaces* **2021**, *13*, 22466.
[14] Y. Zhao, R. Zhou, Z. Song, X. Zhang, T. Zhang, A. Zhou, F. Wu, R. Chen, L. Li, *Angew. Chem., Int. Ed.* **2022**, *61*, 202212231.
[15] S. Guo, S. Liang, B. Zhang, G. Fang, D. Ma, J. Zhou, *ACS Nano* **2019**, *13*, 13456.
[16] L. Ren, G. Yu, H. Xu, W. Wang, Y. Jiang, M. Ji, S. Li, *ACS Sustainable Chem. Eng.* **2021**, *9*, 12223.
[17] Y. Liao, H.-C. Chen, C. Yang, R. Liu, Z. Peng, H. Cao, K. Wang, *Energy Storage Mater.* **2022**, *44*, 508.
[18] Y. Cai, R. Chua, S. Huang, H. Ren, M. Srinivasan, *Chem. Eng. J.* **2020**, *396*, 125221.
[19] J. Ji, J. Yao, Y. Xu, H. Wan, B. Zhang, L. Lv, J. Li, N. Wang, Z. Zheng, J. Zhang, G. Ma, L. Tao, H. Wang, Y. Wang, H. Wang, *Energy Environ. Mater.* **2023**, *6*, e12340.
[20] Y. Ma, M. Xu, R. Liu, H. Xiao, Y. Liu, X. Wang, Y. Huang, G. Yuan, *Energy Storage Mater.* **2022**, *48*, 212.
[21] J. Ji, H. Wan, B. Zhang, C. Wang, Y. Gan, Q. Tan, N. Wang, J. Yao, Z. Zheng, P. Liang, J. Zhang, H. Wang, L. Tao, Y. Wang, D. Chao, H. Wang, *Adv. Energy Mater.* **2021**, *11*, 2003203.
[22] Q. Duan, Y. Wang, S. Dong, D. Y. W. Yu, *J. Power Sources* **2022**, *528*, 231194.
[23] M. E. Pam, D. Yan, J. Yu, D. Fang, L. Guo, X. L. Li, T. C. Li, X. Lu, L. K. Ang, R. Amal, Z. Han, H. Ying Yang, *Adv. Sci.* **2021**, *8*, 2002722.
[24] J. Zhang, W. Li, J. Wang, X. Pu, G. Zhang, S. Wang, N. Wang, X. Li, *Angew. Chem., Int. Ed.* **2023**, *62*, 202215654.
[25] D. Wu, L. M. Housel, S. J. Kim, N. Sadique, C. D. Quilty, L. Wu, R. Tappero, S. L. Nicholas, S. Ehrlich, Y. Zhu, A. C. Marschilok, E. S. Takeuchi, D. C. Bock, K. J. Takeuchi, *Energy Environ. Sci.* **2020**, *13*, 4322.
[26] S. J. Kim, D. Wu, L. M. Housel, L. Wu, K. J. Takeuchi, A. C. Marschilok, E. S. Takeuchi, Y. Zhu, *Chem. Mater.* **2021**, *33*, 7283.
[27] C. Liu, J. Wang, J. Tian, L. Xiang, *J. Nanomater.* **2013**, *2013*, 389634.
[28] M. B. Lim, T. N. Lambert, B. R. Chalamala, *Mater. Sci. Eng. R Rep.* **2021**, *143*, 100593.
[29] B. Lee, H. R. Seo, H. R. Lee, C. S. Yoon, J. H. Kim, K. Y. Chung, B. W. Cho, S. H. Oh, *ChemSusChem* **2016**, *9*, 2948.
[30] Y. Li, Y. Li, Q. Liu, Y. Liu, T. Wang, M. Cui, Y. Ding, H. Li, G. Yu, *Angew. Chem.* **2024**, *136*, 202318444.
[31] A. O. O. Bahdad, Y. Li, T. Van Nguyen, *J. Electrochem. Soc.* **2021**, *168*, 070524.
[32] H. Pan, J. F. Ellis, X. Li, Z. Nie, H. J. Chang, D. Reed, *ACS Appl. Mater. Interfaces* **2019**, *11*, 37524.
[33] C. Julien, M. Massot, S. Rangan, M. Lemal, D. Guyomard, *J. Raman Spectrosc.* **2002**, *33*, 223.
[34] J. E. Post, D. A. McKeown, P. J. Heaney, *Am. Mineral.* **2021**, *106*, 351.
[35] H. Nesbitt, D. Banerjee, *Am. Mineral.* **1998**, *83*, 305.
[36] X. Xiao, Z. Fang, D. Yu, *Front. Mater.* **2019**, *6*, 219.
[37] R. Al-Gaashani, S. Radiman, A. Daud, N. Tabet, Y. Al-Douri, *Ceram. Int.* **2013**, *39*, 2283.
[38] S. Hashimoto, A. Tanaka, *Interfaces Thin Films* **2002**, *34*, 262.
[39] O. Frank, M. Zukalova, B. Laskova, J. Kürti, J. Koltai, L. Kavan, *Phys. Chem. Chem. Phys.* **2012**, *14*, 14567.

[40] L. Jin, L. Xu, C. Morein, C. Chen, M. Lai, S. Dharmarathna, A. Dobley, S. L. Suib, *Adv. Funct. Mater.* **2010**, *20*, 3373.

[41] D. Li, W. Li, Y. Deng, X. Wu, N. Han, Y. Chen, *J. Phys. Chem. C* **2016**, *120*, 10275.

[42] Y. Wu, J. Zhi, M. Han, Z. Liu, Q. Shi, Y. Liu, P. Chen, *Energy Storage Mater.* **2022**, *51*, 599.

[43] L. Liu, Y.-C. Wu, L. Huang, K. Liu, B. Duployer, P. Rozier, P.-L. Taberna, P. Simon, *Adv. Energy Mater.* **2021**, *11*, 2101287.

[44] S. Wang, Z. Yuan, X. Zhang, S. Bi, Z. Zhou, J. Tian, Q. Zhang, Z. Niu, *Angew. Chem.* **2021**, *133*, 7132.

[45] X. Yang, Z. Jia, W. Wu, H.-Y. Shi, Z. Lin, C. Li, X.-X. Liu, X. Sun, *Chem. Commun.* **2022**, *58*, 4845.

[46] T. Sun, Q. Nian, S. Zheng, J. Shi, Z. Tao, *Small* **2020**, *16*, 2000597.

[47] X. Gao, H. Wu, W. Li, Y. Tian, Y. Zhang, H. Wu, L. Yang, G. Zou, H. Hou, X. Ji, *Small* **2020**, *16*, 1905842.

[48] Y. Wu, J. Fee, Z. Tobin, A. Shirazi-Amin, P. Kerns, S. Dissanayake, A. Mirich, S. L. Suib, *ACS Appl. Energy Mater.* **2020**, *3*, 1627.

[49] K. Cai, S. Luo, J. Cong, K. Li, S. Yan, P. Hou, Q. Wang, Y. Zhang, X. Liu, X. Lei, *J. Electrochem. Soc.* **2022**, *169*, 030531.

[50] P. Giannozzi, S. Baroni, N. Bonini, M. Calandra, R. Car, C. Cavazzoni, D. Ceresoli, G. L. Chiarotti, M. Cococcioni, I. Dabo, A. Dal Corso, S. de Gironcoli, S. Fabris, G. Fratesi, R. Gebauer, U. Gerstmann, C. Gougoussis, A. Kokalj, M. Lazzeri, L. Martin-Samos, N. Marzari, F. Mauri, R. Mazzarello, S. Paolini, A. Pasquarello, L. Paulatto, C. Sbraccia, S. Scandolo, G. Sclauzero, A. P. Seitsonen, et al., *J. Phys.: Condens. Matter* **2009**, *21*, 395502.

[51] P. Giannozzi, O. Andreussi, T. Brumme, O. Bunau, M. B. Nardelli, M. Calandra, R. Car, C. Cavazzoni, D. Ceresoli, M. Cococcioni, N. Colonna, I. Carnimeo, A. D. Corso, S. d. Gironcoli, P. Delugas, R. A. DiStasio Jr, A. Ferretti, A. Floris, G. Fratesi, G. Fugallo, R. Gebauer, U. Gerstmann, F. Giustino, T. Gorni, J. Jia, M. Kawamura, H.-Y. Ko, A. Kokalj, E. Küçükbenli, M. Lazzeri, et al., *J. Phys.: Condens. Matter* **2017**, *29*, 465901.

[52] K. F. Garrity, J. W. Bennett, K. M. Rabe, D. Vanderbilt, *Comput. Mater. Sci.* **2014**, *81*, 446.

[53] J. P. Perdew, K. Burke, M. Ernzerhof, *Phys. Rev. Lett.* **1996**, *77*, 3865.

[54] R. W. G. Wyckoff, *Crystal Structures*, 2nd ed., Interscience, New York **1963**.